

In-depth study of long-term variability in the X-ray emission of the Be/X-ray binary system AX J0049.4–7323

L. Ducci^{1,2}, P. Romano³, C. Malacaria¹, L. Ji¹, E. Bozzo², and A. Santangelo¹

¹ Institut für Astronomie und Astrophysik, Kepler Center for Astro and Particle Physics, Eberhard Karls Universität, Sand 1, 72076 Tübingen, Germany

e-mail: ducci@astro.uni-tuebingen.de

² ISDC Data Center for Astrophysics, Université de Genève, 16 chemin d'Écogia, 1290 Versoix, Switzerland

³ INAF – Osservatorio Astronomico di Brera, via Bianchi 46, 23807 Merate (LC), Italy

Received ...; accepted ...

ABSTRACT

AX J0049.4–7323 is a Be/X-ray binary in the Small Magellanic Cloud hosting a ~ 750 s pulsar which has been observed over the last ~ 17 years by several X-ray telescopes. Despite numerous observations, little is known about its X-ray behaviour. Therefore, we coherently analysed archival *Swift*, *Chandra*, *XMM-Newton*, *RXTE*, and *INTEGRAL* data, and we compared them with already published *ASCA* data, to study its X-ray long-term spectral and flux variability. AX J0049.4–7323 shows a high X-ray variability, spanning more than three orders of magnitudes, from $L \approx 1.6 \times 10^{37}$ erg s⁻¹ (0.3–8 keV, $d = 62$ kpc) down to $L \approx 8 \times 10^{33}$ erg s⁻¹. *RXTE*, *Chandra*, *Swift*, and *ASCA* observed, in addition to the expected enhancement of X-ray luminosity at periastron, flux variations by a factor of ~ 270 with peak luminosities of $\approx 2.1 \times 10^{36}$ erg s⁻¹ far from periastron. These properties are difficult to reconcile with the typical long-term variability of Be/XRBs, traditionally interpreted in terms of type I and type II outbursts. The study of AX J0049.4–7323 is complemented with a spectral analysis of *Swift*, *Chandra*, and *XMM-Newton* data which showed a softening trend when the emission becomes fainter, and an analysis of optical/UV data collected by the UVOT telescope on board *Swift*. In addition, we measured a secular spin-up rate of $\dot{P} = (-3.00 \pm 0.12) \times 10^{-3}$ s day⁻¹, which suggests that the pulsar has not yet achieved its equilibrium period. Assuming spherical accretion, we estimated an upper limit for the magnetic field strength of the pulsar of $\approx 3 \times 10^{12}$ G.

Key words. accretion – stars: neutron – X-rays: binaries – X-rays: individuals: AX J0049.4–7323

1. Introduction

AX J0049.4–7323 was discovered by Ueno et al. (2000) in *ASCA* observations of the Small Magellanic Cloud (SMC). It hosts a neutron star (NS) with a pulse period of ≈ 750 s (Yokogawa et al. 2000) and a Be star (Edge & Coe 2003) of spectral type O9.5–B0.5 III–V (McBride et al. 2008). A spectroscopic analysis of the optical counterpart of AX J0049.4–7323 showed a double-peaked H α emission profile, suggesting that the circumstellar disc was observed through the plane of rotation (Edge & Coe 2003). Laycock et al. (2005) and Cowley & Schmidtke (2003) detected a periodicity of ≈ 395 d in X-ray and optical bands interpreted as the orbital period of the NS. Schmidtke et al. (2013) combined MACHO and OGLE data to refine the optical period and ephemeris to $P_{\text{orb}} = 393.1 \pm 0.4$ d and $T_0 = 52979.5 \pm 4$ MJD. Coe & Edge (2004) noticed that the two *RXTE* outbursts (exceeding 3×10^{37} erg s⁻¹ in 3–10 keV, assuming a distance of $d = 62$ kpc) used by Laycock et al. (2005) to estimate the orbital period were synchronized with the optical outbursts. Galache et al. (2008) reported further *RXTE*/PCA detections of AX J0049.4–7323 in outburst, the brightest of which lasted three weeks. AX J0049.4–7323 was also detected by *INTEGRAL* during an outburst that reached an X-ray luminosity $\gtrsim 10^{37}$ erg s⁻¹ (Coe et al. 2010). AX J0049.4–7323 was also detected three times by *ASCA*. In all these cases, it was observed far from the optical outbursts and it showed an X-ray luminosity of 5×10^{35} erg s⁻¹ (Coe & Edge 2004). An analysis of archival

ROSAT and *Einstein* data showed AX J0049.4–7323 at a relatively low luminosity level ($\leq 5 \times 10^{35}$ erg s⁻¹) for over 20 years (Yokogawa et al. 2000). As noted by Coe & Edge (2004), the three *ASCA* detections at high X-ray luminosities were difficult to explain in the context of the typical variability displayed by Be/X-ray binaries (Be/XRBs). In general, Be/XRBs are transient X-ray sources with high eccentric orbits ($e \gtrsim 0.3$; Reig 2011). The bright X-ray events characterizing the X-ray variability of Be/XRBs are schematically divided into two groups, called type I and type II outbursts. Type I outbursts are periodic (or quasi-periodic) events, occurring in correspondence with the periastron. They last for a small fraction of the orbit ($0.2\text{--}0.3 P_{\text{orb}}$) and their maximum luminosity is typically of the order of $\lesssim 10^{37}$ erg s⁻¹. They exceed at least two orders of magnitude with respect to the quiescent state, when the luminosity is $\lesssim 10^{35}$ erg s⁻¹. Type II outbursts are not periodic and can peak at any orbital phase. They are brighter than type I outbursts and can reach X-ray luminosities of $\approx 10^{38}$ erg s⁻¹. They last for a large fraction of the orbit or for several orbital periods (Reig 2011). Tidal and resonant interactions of the NS with the circumstellar disc can lead to the truncation of the latter at a radial distance which depends on the viscosity of the disc (Okazaki & Negueruela 2001; Negueruela & Okazaki 2001). In binary systems with low eccentricity ($e \lesssim 0.2$), the gap size between the outer radius of the truncated disc and the orbit is so large that no type I outbursts occur. These systems show only type II outbursts and only occasionally type I outbursts, when

the disc is strongly disturbed (Reig 2011). In binary systems with high eccentricity ($e \gtrsim 0.6$) the disc truncation is not efficient. At every periastron passage, the mass accretion rate is large enough to cause regular type I outbursts (Okazaki & Negueruela 2001). For systems with moderate eccentricity, the situation is more complicated. The global properties of their X-ray variability depend more closely on the orbital separation and viscosity properties of the circumstellar disc (Okazaki & Negueruela 2001). The ASCA detections at luminosities of $5 \times 10^{35} \text{ erg s}^{-1}$ could not be classified as type I because they were not observed at periastron and they were not bright enough for type II (Coe & Edge 2004). The observations in hand of Coe & Edge (2004) were insufficient to draw further conclusions about the anomalous X-ray behaviour shown by AX J0049.4–7323. Therefore, the aim of this work is to provide a detailed analysis of the largest possible set of X-ray data to infer more information about the main properties of this system through a global study of the X-ray long-term flux and spectral variability. We coherently analysed *Swift* (XRT and UVOT), *Chandra*, *XMM-Newton*, *RXTE*, and *INTEGRAL* data (collected over the last ~ 17 years and corresponding to a total exposure time of ~ 5.86 Ms; Sect. 2). The results are presented in Sect. 3 and discussed in Sect. 4.

2. Reduction and data analysis

2.1. *Swift*

The SMC has been observed repeatedly with *Swift* (Gehrels et al. 2004) since its launch; in particular, starting on 2016 June 8, the SMC has been observed as part of the *Swift* survey of the Small Magellanic Cloud (Kennea et al. 2016). Therefore, we collected all observations in which the source was within the field of view of the narrow-field instruments, the X-ray Telescope (XRT, Burrows et al. 2005) and the UV/Optical Telescope (UVOT, Roming et al. 2005). The observations are listed in Table 1.

The XRT data were uniformly processed and analysed using the standard software (FTOOLS¹ v6.20), calibration (CALDB² 20170501), and methods. We used the task XRTPIPELINE (v0.13.3) to process and filter the XRT data, and extracted source events from a circular region with a radius of 10 pixels (1 pixel corresponds to $2.36''$). Background events were extracted in most cases from an annular region with an inner radius of 30 pixels and an external radius of 70 pixels centred at the source position, the exception being when the source was close to the edge of the FOV; in this case we used a circular region (with a radius of 50 to 70 pixels). The data are not affected by pile-up. The XRT light curve was corrected for PSF losses and vignetting and background subtracted. For the spectral analysis, we extracted events in the regions described above. Then, we used xrtmkarf to generate ancillary response files that account for different extraction regions, vignetting, and PSF corrections. Spectra were extracted in each individual observation and in several datasets combined. All were binned at 1 count per bin and fit adopting Cash (Cash 1979) statistics.

When no detection was achieved, the corresponding 3σ upper limit on the X-ray count rate was estimated by using the tasks *sosta* and *uplimit* within XIMAGE (with the background calculated in the neighbourhood of the source position) and the Bayesian method for low-count experiments adapted from Kraft et al. (1991).

¹ https://heasarc.gsfc.nasa.gov/ftools/ftools_menu.html.

² https://heasarc.gsfc.nasa.gov/docs/heasarc/caldb/caldb_intro.html.

UVOT observed the target simultaneously with XRT. As the observations were obtained from the *Swift* archive, there is no uniformity of filter usage in the UVOT data. The data analysis was performed using the *uvotimsum* and *uvotsource* tasks included in FTOOLS. The *uvotsource* task calculates the magnitude of the source through aperture photometry within a circular region centred on the best source position and applies the required corrections related to the specific detector characteristics. We adopted a circular region with a radius of $5''$ for the photometry of the different sources. The background was evaluated in all cases by using circular regions with a radius of $10''$. For the magnitude uncertainties, we added in quadrature the systematic errors provided by UVOTSOURCE.

2.2. *Chandra*

Chandra data have been explored to analyse the long-term behaviour of AX J0049.4–7323. We extracted images for each of the *Chandra* observations in which the source was detected within the ACIS field of view (see Table 3). We applied the latest *Chandra* calibration files to each image and we reduced the data with the *Chandra* Interactive Analysis of Observations software package (CIAO, version 4.9). Source fluxes were extracted with the CIAO tool *srcflux* (Glotfelty 2014). We extracted source events from circular regions with radius of about $3'' - 5''$, while the background was extracted from an annular region around the source, with internal radius as large as twice that of the source region and outer radius equal to about 5 times the source radius. The extraction energy band was constrained to $0.3 - 8 \text{ keV}$. Due to the low count rates detected from this source and its peripheral position on the ACIS detectors (which smears the detection region), pile-up effects are negligible (pile-up fraction generally $< 1\%$). *Chandra* spectra have been extracted using the CIAO *specextract* tool and analysed using XSPEC (ver. 12.9.1, Arnaud 1996). Spectral channels were rebinned to contain at least 25 photons per energy bin.

2.3. *XMM-Newton*

XMM-Newton observed three times the field around AX J0049.4–7323: 2000-10-15 15:09:54 (UTC), 2007-04-11 19:37:46, and 2009-10-03 05:08:04 (see Table 3). The data analysis of each observation was performed through the *XMM-Newton* Science Analysis System (SAS) software (version 15.0.0). Time intervals affected by high background were excluded, and calibrated event lists for pn, MOS1, and MOS2 were produced using the *epproc* and *emproc* tasks. For the pn data we used single- and double-pixel events (PATTERN ≤ 4), while for the MOS data, single-pixel to quadruple-pixel events (PATTERN ≤ 12) were used. For each observation we extracted in each detector the source events in circular regions centred on the target, using appropriate radii, according to the brightness of the source and its location in the detector. Background events were accumulated from source-free circular regions far from the point spread function of the source. We extracted the spectra of the first two observations. Spectral channels were rebinned to contain at least 25 photons per energy bin. For each observation, we fitted all the available EPIC spectra simultaneously using XSPEC.

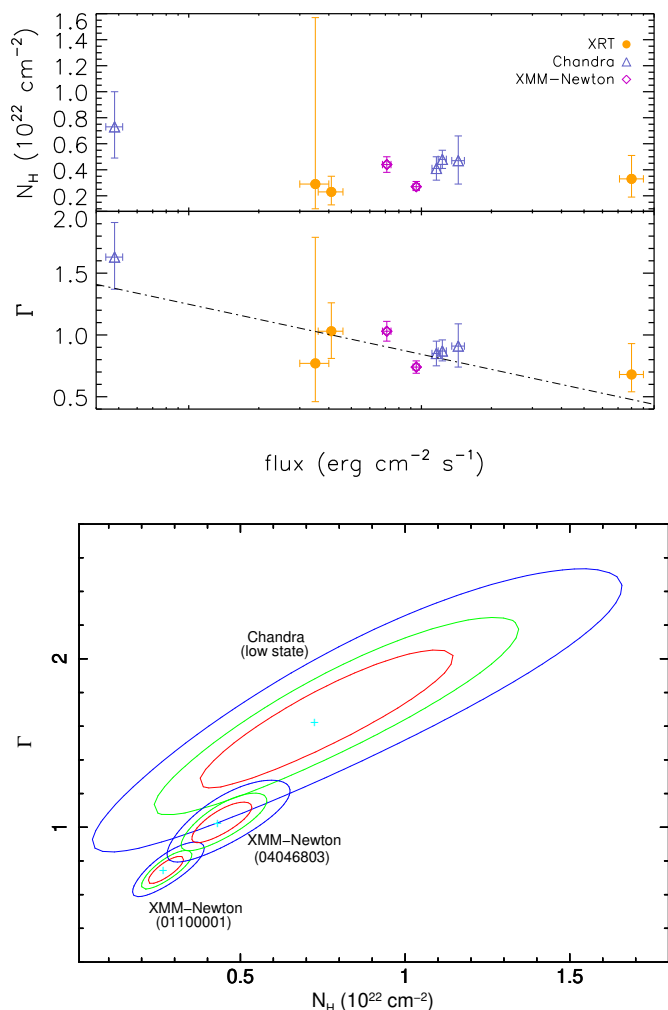


Fig. 1. *Top panel:* Column density and photon index as a function of the absorbed flux (errors quoted at 1σ c.l.). The plotted values correspond to those listed in Table 3. The anti-correlation Γ vs flux is emphasized by the dot-dashed line, which shows the best linear fit (Γ vs $\log_{10} F_x$). *Bottom panel:* Confidence contours at 68%, 95%, and 99% in the N_{H} – Γ plane of the *Chandra* spectrum at the lowest luminosity level and the *XMM-Newton* spectra.

servations with insufficient statistics to perform a spectral analysis, we reported in Table 3 the flux in the range 0.3–8 keV obtained from the conversion of the count rate, assuming an absorbed power law spectrum with $N_{\text{H}} = 4 \times 10^{21} \text{ cm}^{-2}$ and photon index of 0.8. The results of the spectral analysis of the two *XMM-Newton* observations 0110000101 and 0404680301 and the *Chandra* observations 8479, 7156, and 8481 are consistent, within the 90% confidence level (c.l.) with those reported in Haberl & Pietsch (2004); Haberl et al. (2008), and Hong et al. (2017). The observed X-ray fluxes are also consistent with those reported by Yang et al. (2017). The results from the other observations are published here for the first time. The slopes of the power law given in Table 3 are typical of accreting pulsars.

We grouped the *Chandra* observations of the source detected at the lowest luminosity state (when $F_x < 10^{-12} \text{ erg cm}^{-2} \text{ s}^{-1}$) to perform a meaningful spectral analysis. The resulting average spectrum can be fitted with an absorbed power law model with $N_{\text{H}} = 0.73^{+0.26}_{-0.24} 10^{22} \text{ cm}^{-2}$, $\Gamma = 1.63^{+0.28}_{-0.26}$, $\chi^2_{\nu} = 1.23$ (11 d.o.f.). The power law slope is higher than in the observations where the source is detected at higher fluxes (Table 3).

The upper panel of Fig. 1 shows the values of N_{H} and Γ in Table 3 as a function of the absorbed flux. The plot shows that the spectral slope softens at lower fluxes ($\Gamma = (-4.0 \pm 1.7) \times \log_{10} F_x - (0.4 \pm 0.14)$, errors quoted at 1σ c.l.). To quantify the significance of the anticorrelation Γ versus flux, we calculated the Pearson’s linear coefficient r and the null hypothesis probability p in the $\log_{10} x - y$ space. We found $r = -0.83$ and $p = 0.5\%$. The parameter N_{H} does not show a significant correlation with flux; in fact, a linear fit of N_{H} versus $\log_{10} F_x$ results in $N_{\text{H}} \propto (0.17 \pm 0.22) \times \log_{10} F_x$, where the error is quoted at 2σ c.l. The slope is thus consistent with zero at 2σ c.l. To highlight the significant spectral variability of AX J0049.4–7323, we show in Fig. 1, lower panel, the 68%, 95%, and 99% confidence contours in the N_{H} – Γ plane of the average *Chandra* spectrum at the lowest luminosity level (the ‘combined’ spectrum in Table 3) and the *XMM-Newton* spectra where the flux was up to ~ 20 times larger.

3.2. Timing analysis

We used the Lomb–Scargle periodogram technique (Press & Rybicki 1989) to search for periodicities in *XMM-Newton*, *Chandra*, and *RXTE* data. *Swift* observations were too short compared to the spin period of AX J0049.4–7323 to search for periodicities. For *RXTE* data, we performed timing analysis in each observation and in groups of observations within one day. We searched for periodicities within a small window ranging from 720 s to 780 s. We set the limits of this window on the basis of the spin period history of the source reported by Yang et al. (2017). We set a false alarm probability of detection of 99.9%. The number of independent trial frequencies was calculated according to equation 13 of Horne & Baliunas (1986). We detected pulsations in the *XMM-Newton* observations 0110000101 and 0404680301, and in the *Chandra* observations 8479, 7156, and 8481. For these observations, our measurements of the spin period are in agreement with those reported in Haberl et al. (2008) and Hong et al. (2017), hence hereafter we use the *Chandra* and *XMM-Newton* spin periods published in those papers. In the other *Chandra* and *XMM-Newton* observations we did not detect any pulsating signal probably because of the insufficient statistics (see Sect. 4.2.1). We detected AX J0049.4–7323 in the *RXTE* observations reported in Table 2. Figure 2 shows the long-term spin period evolution of AX J0049.4–7323. In addition to the spin period measurements obtained in this work, we included the spin period measured by Yokogawa et al. (2000) using *ASCA* ($P_{\text{ASCA}} = 755.5 \pm 0.6$ s). Figure 2 shows a significant long-term spin-up of $\dot{P} = (-3.00 \pm 0.12) \times 10^{-3} \text{ s day}^{-1}$.

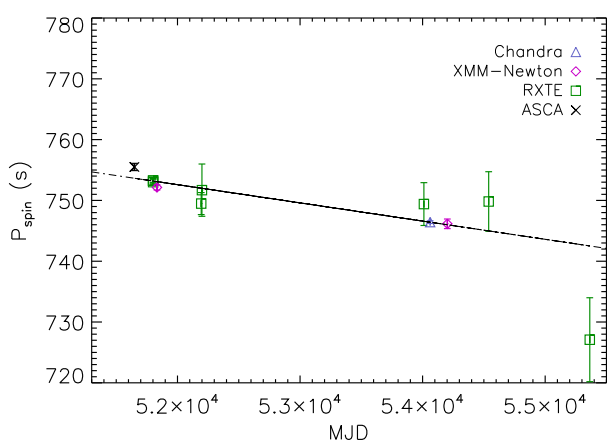
The source does not show significant variability such as flares within each observation, in agreement with previous findings obtained by Hong et al. (2017), Haberl et al. (2008), and Haberl & Pietsch (2004), based on *Chandra* and *XMM-Newton* data.

3.3. Long-term flux variability

Figure 3 shows the long-term flux history of AX J0049.4–7323, from 2000 April 11 to 2017 March 15, based on *Swift*/*XRT*, *Chandra*, *XMM-Newton*, *RXTE*/*PCA*, *INTEGRAL*, and *ASCA* data. Each point, except for *INTEGRAL*, represents the average 0.3–8 keV flux measured during the different observations. For *INTEGRAL*, sky images of each pointing were generated in the energy band 20 – 40 keV. AX J0049.4–7323 was never

Table 2. Measurements of the spin period and 0.3–8 keV flux of AX J0049.4–7323 in *RXTE* observations.

T_{start}	T_{stop}	P_{spin}	F_x
MJD	MJD	(s)	($10^{-11} \text{ erg cm}^{-2} \text{ s}^{-1}$)
51800.00	51800.70	753.24 ± 0.42	1.75 ± 0.16
51800.86	51801.30	753.00 ± 0.41	1.62 ± 0.16
51801.44	51802.28	753.28 ± 0.31	1.48 ± 0.16
52193.617	52193.76	749.48 ± 1.81	3.50 ± 0.16
52199.47	52199.57	751.686 ± 4.3	1.25 ± 0.16
54010.46	54010.73	749.398 ± 3.52	0.46 ± 0.16
54539.03	54539.14	749.82 ± 4.9	1.21 ± 0.16
55363.906	55364.087	727.09 ± 6.9	0.43 ± 0.16

**Fig. 2.** Spin period evolution of AX J0049.4–7323. The black line shows the best-fit long-term spin-up. Error bars indicate 1σ uncertainties.

detected, being below the 5σ threshold of detection, in the individual sky images of each pointing. Then, for each *INTEGRAL* revolution, we combined the individual images to produce mosaic images. As already shown in Coe et al. (2010), AX J0049.4–7323 is detected with a significance of 6.9σ during the *INTEGRAL* revolution 796, corresponding to the time interval 54941.368–54942.975 MJD and orbital phase $\phi = 0.992$. The 20–40 keV is $F_x = (3.8 \pm 0.6) \times 10^{-11} \text{ erg cm}^{-2} \text{ s}^{-1}$, corresponding to a luminosity of $(1.7 \pm 0.3) \times 10^{37} \text{ erg s}^{-1}$. AX J0049.4–7323 was never detected in the other revolution-based mosaic images. It has been observed with a long exposure (429 ks) during the periastron passage ~ 57316 – 57335 MJD. We measured a 20–40 keV 3σ flux upper limit of $9.8 \times 10^{-12} \text{ erg cm}^{-2} \text{ s}^{-1}$.

For *RXTE* data, we used equation 5 of Yang et al. (2017) to calculate, from each pulsation amplitude and corresponding uncertainty, the 0.3–8 keV flux of the source. We converted the flux from units counts/PCU/s to $\text{erg cm}^{-2} \text{ s}^{-1}$ using PIMMS and assuming an absorbed power law model with $N_{\text{H}} = 4 \times 10^{21} \text{ cm}^{-2}$ and a photon index of 0.8. For the pulsed fraction, we assumed, in accordance with Yang et al. (2017) and the typical values of AX J0049.4–7323 (Hong et al. 2017), $p_f = 0.4$. The *RXTE* fluxes depend on the spectral and pulsed fraction parameters reported above, which are variable. Therefore, *RXTE*

fluxes could be subject to large uncertainties. By varying the spectral parameters and p_f according to Table 3 and Hong et al. (2017) and Haberl et al. (2008), we find that the *RXTE* fluxes are known with a relative uncertainty of $\sim 50\%$. Figure 3 shows that *RXTE* data have a systematically higher flux than the observations from other instruments, also when the relative uncertainties of $\sim 50\%$ of *RXTE* fluxes are taken into account. This is a selection bias caused by the larger number of *RXTE*/PCA observations with AX J0049.4–7323 in the field of view (391, Yang et al. 2017) compared to the low number of observations from other telescopes, together with the relatively low sensitivity of *RXTE*/PCA (flux threshold: $\approx 4 \times 10^{-12} \text{ erg cm}^{-2} \text{ s}^{-1}$ in the 2–10 keV energy band; Jahoda et al. 1996). In addition to *Swift*, *XMM-Newton*, *Chandra*, and *RXTE*, we plotted the *ASCA* fluxes reported in Yokogawa et al. (2000) and converted to the 0.3–8 keV energy range assuming an absorbed power law spectrum with the parameters found by Yokogawa et al. (2000) during the *ASCA* observations. *INTEGRAL* data of Fig. 4 are instead in the 20–40 keV energy range.

AX J0049.4–7323 shows a high X-ray variability, spanning more than three orders of magnitude, from $\sim 1.7 \times 10^{-14} \text{ erg cm}^{-2} \text{ s}^{-1}$ (corresponding to a luminosity of $L_x \sim 8 \times 10^{33} \text{ erg s}^{-1}$ in the energy range 0.3–8 keV) to $\sim 3.5 \times 10^{-11} \text{ erg cm}^{-2} \text{ s}^{-1}$ ($L_x \sim 1.6 \times 10^{37} \text{ erg s}^{-1}$). We found that, in addition to *ASCA* (Coe & Edge 2004), *Swift*, *RXTE*, and *Chandra* also observed AX J0049.4–7323 at orbital phases not coinciding with the periastron during relatively high luminosity states ($L_x > 2 \times 10^{35} \text{ erg s}^{-1}$).

Figure 4 shows the X-ray light curve folded at the orbital period of AX J0049.4–7323 (we adopted the ephemeris calculated by Schmidtke et al. 2013). At periastron ($0.02 \lesssim \phi \lesssim 0.98$) the flux is on average higher than elsewhere and varies by a factor of ~ 4 , from $F_x \approx 8 \times 10^{-12} \text{ erg cm}^{-2} \text{ s}^{-1}$ ($L_x \approx 3.7 \times 10^{36} \text{ erg s}^{-1}$) to $F_x \approx 3.5 \times 10^{-11} \text{ erg cm}^{-2} \text{ s}^{-1}$ ($L_x \approx 1.6 \times 10^{37} \text{ erg s}^{-1}$). Outside the periastron passage, the maximum variability factor is ≈ 270 , and the flux (luminosity) ranges from $F_x \approx 1.7 \times 10^{-14} \text{ erg cm}^{-2} \text{ s}^{-1}$ ($L_x \approx 8 \times 10^{33} \text{ erg s}^{-1}$) to $F_x \approx 4.6 \times 10^{-12} \text{ erg cm}^{-2} \text{ s}^{-1}$ ($L_x \approx 2.1 \times 10^{36} \text{ erg s}^{-1}$). The light curve does not show a sinusoidal modulation. On the contrary, it is characterized (see also Fig. 3) by jumps in luminosity apparently uniformly distributed across the orbit rather than being clustered at some particular orbital phase.

3.4. UVOT

Figure 5 shows the UVOT light curves in four filters (U: 3465 Å; W1: 2600 Å; M2: 2246 Å; W2: 1928 Å) folded at the orbital period (see Sect. 3.3). Clearly, AX J0049.4–7323 is significantly variable in all bands, with amplitudes $\Delta m_U = 0.1$, $\Delta m_{W1} = 0.16$, $\Delta m_{M2} = 0.15$, and $\Delta m_{W2} = 0.07$. Unfortunately, the data are too sparse to draw any conclusion about the UV variability along the orbit of AX J0049.4–7323.

4. Discussion

4.1. Secular spin-up

Our data analysis of *RXTE* data led to a lower number of detections compared to the works of Klus et al. (2014) and Yang et al. (2017). This is due to the highest threshold of detection adopted in our work (99.9% versus 99%) and to the different data analysis reduction (for the sophisticated data analysis procedure adopted by Klus et al. (2014) and Yang et al. (2017), see Galache et al. 2008). Since we set a higher detection threshold

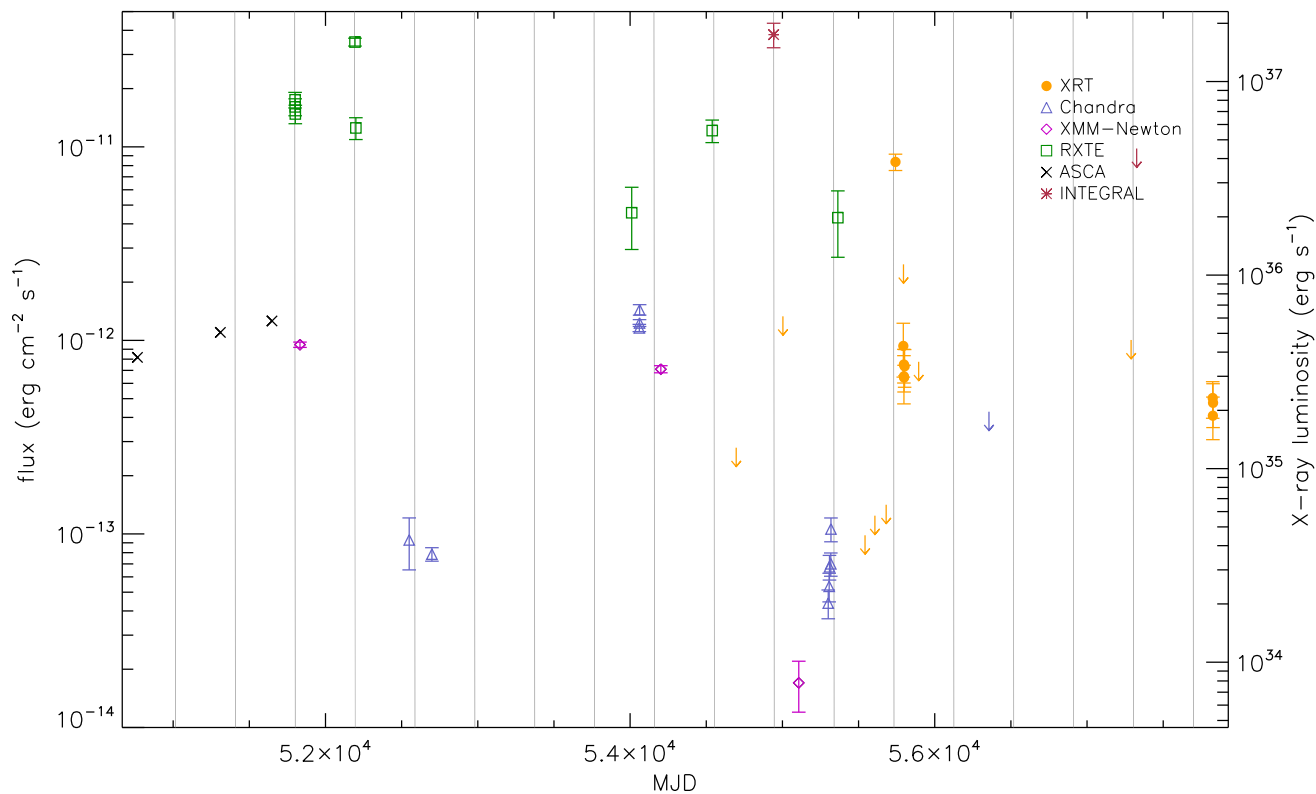


Fig. 3. X-ray light curve (0.3–8 keV) of AX J0049.4–7323 obtained from *Swift*/XRT, *Chandra*, *XMM-Newton*, and *RXTE* data analysed in this work, and *ASCA* data from [Yokogawa et al. \(2000\)](#). *INTEGRAL* points are in the energy range 20–40 keV. Downward arrows are used to indicate 3σ upper limits. Grey vertical lines show the times of periastron passages according to the ephemeris calculated by [Schmidtke et al. \(2013\)](#). The right y-axis shows the absorbed 0.3 – 8 keV X-ray luminosity, assuming $d = 62$ kpc. Error bars indicate the 1σ uncertainties.

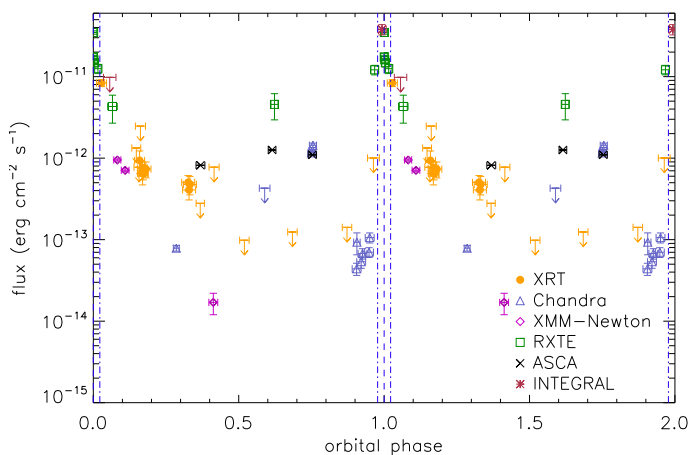


Fig. 4. *Swift*, *Chandra*, *XMM-Newton*, and *RXTE* 0.3–8 keV fluxes folded at the orbital period of AX J0049.4–7323. *INTEGRAL* points are in the energy range 20–40 keV. Downward arrows are used to indicate 3σ upper limits. Vertical dashed lines and dot-dashed lines show the position of the periastron passages and their uncertainties, respectively.

in the Lomb–Scargle analysis, we consider only the strongest signals. Our measurements are thus less contaminated by other signals (e.g. from other pulsars of the SMC in the field of view of AX J0049.4–7323) which could lead to lower precision and accuracy of the measurements. The improvement obtained by the increase in the detection threshold can be seen in Fig 2 where the

values of the spin periods are less scattered than they are in the plots of [Klus et al. \(2014\)](#) (figure B39) and [Yang et al. \(2017\)](#)⁴.

AX J0049.4–7323 shows a long-term spin-up rate of $\dot{P} = (-3.00 \pm 0.12) \times 10^{-3} \text{ s day}^{-1}$, which is more precise than the spin-up rate reported in [Yang et al. \(2017\)](#) [$\dot{P} = (-4.1 \pm 1.6) \times 10^{-3} \text{ s day}^{-1}$]. Such high secular spin-up, when compared with those of other accreting pulsars, indicates that the pulsar of AX J0049.4–7323 is likely far from its equilibrium period. For comparison, the Be/XRB SAX J2103.5+4545 has shown, since its discovery in 1997, a secular spin-up of $\dot{P} \approx -1.2 \times 10^{-3} \text{ s day}^{-1}$ ([Camero et al. 2014](#)) and it is believed that it has not yet reached its equilibrium period ([Baykal et al. 2002](#)). If the pulsar of AX J0049.4–7323 were in equilibrium, it would be possible to obtain an estimate of its magnetic field strength (see e.g. [Klus et al. 2014](#)). Since AX J0049.4–7323 is not in equilibrium, we can just calculate an upper limit for its magnetic field. For this purpose, we used the calculations presented in [Ikhsanov \(2007\)](#) to show that slow pulsars ($P_{\text{spin}} \sim 10^2 - 10^4 \text{ s}$) in equilibrium do not need supercritical initial magnetic fields of the NS ($B \geq B_{\text{cr}} \approx 4.4 \times 10^{13} \text{ G}$). Adapting the calculations presented for the spherical accretion scenario (see equation 8 in [Ikhsanov 2007](#)), the maximum magnetic field of AX J0049.4–7323 would

⁴ See <https://authortools.aas.org/AAS03548/FS9/figset.html>

Table 3. Spectral parameters and fluxes of the *XMM-Newton*, *Swift*, and *Chandra* observations analysed in this work. For observations for which spectral analysis was possible, we reported the unabsorbed luminosity.

<i>XMM-Newton</i>											
MJD	ObsID	Exposure [ks]			N_{H}	Γ	χ^2_{ν} (d.o.f.)	absorbed flux	unabs. flux	L_x	Orb. phase
		pn	mos1	mos2	10^{22} cm^{-2}			(0.3–8 keV) $\text{erg cm}^{-2} \text{ s}^{-1}$	(0.3–8 keV) erg s^{-1}		
51832.63	0110000101	15.9	23.7	22.1	$0.27^{+0.04}_{-0.03}$	0.74 ± 0.05	0.892 (115)	$9.5 \pm 0.3 \times 10^{-13}$	$10.4^{+0.3}_{-0.3} \times 10^{-13}$	$4.48^{+0.15}_{-0.14} \times 10^{35}$	0.082
54201.83	0404680301	13.0			$0.44^{+0.06}_{-0.06}$	1.03 ± 0.08	1.168 (47)	$7.1 \pm 0.3 \times 10^{-13}$	$8.4^{+0.3}_{-0.4} \times 10^{-13}$	$3.63^{+0.14}_{-0.16} \times 10^{35}$	0.109
55107.21	0601211301			31.2				$1.7 \pm 0.5 \times 10^{-14}$			0.413
<i>Swift</i>											
MJD	ObsID	Exposure [ks]		N_{H}	Γ	$C - \text{stat}$ (d.o.f.) g-o-f	absorbed flux	unabs. flux	L_x	Orb. phase	
		XRT/PC		10^{22} cm^{-2}			(0.3–8 keV) $\text{erg cm}^{-2} \text{ s}^{-1}$	(0.3–8 keV) erg s^{-1}			
54696.456	00037787001	3.1					$< 2.8 \times 10^{-13} *$			0.368	
55003.093	00031428001	0.6					$< 1.3 \times 10^{-12} *$			0.148	
55542.323	00090522001	9.9					$< 9.8 \times 10^{-14} *$			0.520	
55607.252	combined ⁵	10.5					$< 1.2 \times 10^{-13} *$			0.685	
55681.016	00090522005	10.0					$< 1.4 \times 10^{-13} *$			0.872	
55742.18	00040442001	2.26		$0.33^{+0.18}_{-0.14}$	$0.68^{+0.25}_{-0.24}$	93.18 (121); 87.82%	$8.0^{+1.0}_{-0.9} \times 10^{-12}$	$8.8^{+1.0}_{-0.9} \times 10^{-12}$	$4.0^{+0.5}_{-0.4} \times 10^{36}$	0.028	
55792.999	combined ⁶	2.5					$< 7.7 \times 10^{-13} *$			0.157	
55793.768	00040440001	1.6					$9.4 \pm 2.9 \times 10^{-13}$			0.159	
55794.905	00040440002	0.2					$< 2.5 \times 10^{-12} *$			0.162	
55796.30	combined ¹	21.36		$0.23^{+0.12}_{-0.10}$	$1.03^{+0.23}_{-0.22}$	95.89 (113); 97.77%	$4.1^{+0.5}_{-0.5} \times 10^{-13}$	$4.7^{+0.5}_{-0.5} \times 10^{-13}$	$2.4^{+0.2}_{-0.2} \times 10^{35}$	0.166	
55797.507	00032075002	6.3					$7.5 \pm 1.5 \times 10^{-13}$			0.1687	
55797.747	00032080001	2.9					$6.5 \pm 1.8 \times 10^{-13}$			0.1693	
55798.638	00032075003	10.5					$6.4 \pm 1.0 \times 10^{-13}$			0.172	
55802.352	combined ⁴	4.1					$7.3 \pm 1.6 \times 10^{-13}$			0.181	
55894.422	00032194001	0.9					$< 7.8 \times 10^{-13} *$			0.415	
57289.163	00034071001	0.4					$< 1.0 \times 10^{-12} *$			0.963	
57824.949	00088083001	7.2					$5.0 \pm 1.1 \times 10^{-13}$			0.326	
57825.78	combined ²	21.84		$0.29^{+1.28}_{-0.19}$	$0.77^{+1.02}_{-0.31}$	58.72 (76); 98.69%	$3.5^{+0.5}_{-0.5} \times 10^{-13}$	$3.9^{+3.0}_{-0.5} \times 10^{-13}$	$1.8^{+1.4}_{-0.2} \times 10^{35}$	0.328	
57826.139	00088083002	7.3					$4.1 \pm 1.0 \times 10^{-13}$			0.329	
57827.275	00088083003	7.3					$4.8 \pm 1.2 \times 10^{-13}$			0.332	
<i>Chandra</i>											
MJD	ObsID	Exposure [ks]		N_{H}	Γ	χ^2_{ν} (d.o.f.)	absorbed flux	unabs. flux	L_x	Orb. phase	
		ACIS-S / -I		10^{22} cm^{-2}			(0.3–8 keV) $\text{erg cm}^{-2} \text{ s}^{-1}$	(0.3–8 keV) erg s^{-1}			
52549.6	2945	11.7 (ACIS-S)					$9.3^{+3.1}_{-2.5} \times 10^{-14}$			0.906	
52698.6	3907	50.8 (ACIS-S)					$7.9^{+0.6}_{-0.6} \times 10^{-14}$			0.285	
54060.5	8479	42.6 (ACIS-I)		$0.41^{+0.09}_{-0.09}$	$0.85^{+0.10}_{-0.10}$	1.081 (47)	$1.16^{+0.05}_{-0.05} \times 10^{-12}$	$1.37^{+0.05}_{-0.05} \times 10^{-12}$	$6.3^{+0.2}_{-0.2} \times 10^{35}$	0.750	
54061.8	7156	39.2 (ACIS-I)		$0.48^{+0.07}_{-0.07}$	$0.87^{+0.09}_{-0.08}$	1.089 (56)	$1.23^{+0.05}_{-0.05} \times 10^{-12}$	$1.43^{+0.05}_{-0.05} \times 10^{-12}$	$6.6^{+0.2}_{-0.2} \times 10^{35}$	0.753	
54062.6	8481	16.2 (ACIS-I)		$0.47^{+0.19}_{-0.18}$	$0.91^{+0.18}_{-0.17}$	0.974 (22)	$1.44^{+0.09}_{-0.09} \times 10^{-12}$	$1.68^{+0.10}_{-0.09} \times 10^{-12}$	$7.7^{+8.2}_{-7.3} \times 10^{35}$	0.755	
55300.9	11097	29.9 (ACIS-S)					$4.4^{+0.8}_{-0.7} \times 10^{-14}$			0.905	
55307.1	11980	23.0 (ACIS-S)					$5.4^{+1.0}_{-0.9} \times 10^{-14}$			0.921	
55308.9	12200	27.1 (ACIS-S)					$6.8^{+1.0}_{-1.0} \times 10^{-14}$			0.926	
55317.7	11981	34.0 (ACIS-S)					$7.0^{+1.0}_{-1.0} \times 10^{-14}$			0.948	
55318.6	12208	16.2 (ACIS-S)					$1.1^{+0.2}_{-0.2} \times 10^{-13}$			0.950	
56355.9	14674	46.5 (ACIS-S)					$< 2.3 \times 10^{-13} *$			0.589	
	combined ³	239.2 (ACIS-S)		$0.73^{+0.27}_{-0.24}$	$1.63^{+0.28}_{-0.26}$	1.237 (11)	$4.8^{+0.4}_{-0.4} \times 10^{-14}$	$7.6^{+1.6}_{-6.0} \times 10^{-14}$			

Notes. ¹: ObsID of the combined observations: 00040440001, 00032075002, 00032080001, 00032075003. ²: ObsID of the combined observations: 00088083001, 00088083002, 00088083003. ³: ObsID of the combined observations: 3907, 2945, 11097, 11980, 12200, 11981, 12208. ⁴: ObsID of the combined observations: 00040462002, 00040462003, 00040439002, 00040440003, 00040439003. ⁵: ObsID of the combined observations: 00090522002, 00090522003, 00090522004. ⁶: ObsID of the combined observations: 00040462001, 00040439001. * 3σ upper limit.

be

$$B_{\text{sph}} \lesssim 2.7 \times 10^{10} P_{\text{eq}} k_t^{-1/2} \xi_{0.2}^{1/2} M_{1.4} L_{37}^{1/2} \times \left(\frac{v_{\text{rel}}}{400 \text{ km s}^{-1}} \right)^{-2} \left(\frac{P_{\text{orb}}}{250 \text{ d}} \right)^{-1/2} \approx 3 \times 10^{12} \text{ G}, \quad (1)$$

where k_t is a parameter of the order of unity (Ikhsanov 2007; Ikhsanov et al. 2002), $M_{1.4} = M_{\text{NS}}/(1.4M_{\odot})$ is the mass of the NS, L_{37} is the X-ray luminosity in units of $10^{37} \text{ erg s}^{-1}$, v_{rel} is the relative velocity between the NS and the wind from the com-

panion star, and $\xi_{0.2} = \xi/0.2$ is a factor that takes into account the reduction of the angular momentum accretion rate caused by velocity and density inhomogeneities in the accretion flow (see Ikhsanov 2007 and references therein). Since the pulsar of AX J0049.4–7323 is not in equilibrium, we calculated the upper limit B_{sph} for the conservative case of $P_{\text{eq}} = 750 \text{ s}$, and we assumed an average luminosity of $\sim 4 \times 10^{35} \text{ erg s}^{-1}$. We obtained it from the *Swift*, *Chandra*, *XMM-Newton*, and *ASCA* observations. We did not consider the *RXTE* observations because they

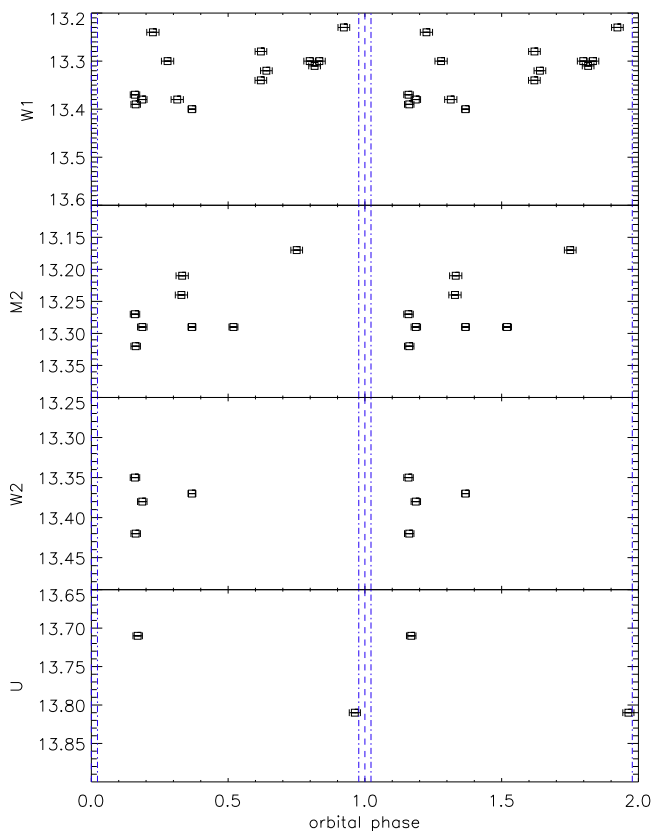


Fig. 5. UVOT observations folded at the orbital period of AX J0049.4–7323. Downward arrows are used to indicate 3σ upper limits. Vertical dashed lines and dot-dashed lines show the position of the periastron passages and their uncertainties, respectively.

would introduce a bias due to the relatively low sensitivity of PCA compared to the other three instruments.

Ikhsanov (2007) pointed out that the probability of observing in X-ray a long-period accreting pulsar fed by an accretion disc at a rate of $\sim 10^{15} \text{ g s}^{-1}$ is very low because the accretion disc would spin up the pulsar at a high rate, implying a lifetime of the pulsar during the accretion phase of $\ll 1000 \text{ yr}$, i.e. several orders of magnitude smaller than the typical lifetime of accreting NSs in high-mass X-ray binaries. Therefore, according to Ikhsanov (2007), the accretion disc scenario is unlikely for binary systems similar to AX J0049.4–7323. Nonetheless, we considered here, for completeness, also this case. From equation 7 in Ikhsanov (2007), the upper limit of the magnetic field in the accretion disc case would be

$$B_{\text{disc}} \lesssim 4.2 \times 10^{11} P_{\text{eq}}^{7/6} \kappa_{0.5}^{7/24} k_t^{-7/12} M_{1.4}^{1/3} L_{37}^{1/2} \approx 2 \times 10^{14} \text{ G}, \quad (2)$$

where $\kappa_{0.5} = \kappa/0.5$ is a parameter that takes into account the geometry of the accretion flow ($\kappa = 0.5$ corresponds to disc geometry, while $\kappa = 1$ to the spherical geometry). We assumed the same P_{eq} and L_{37} of the spherical accretion case.

4.2. Long-term variability

AX J0049.4–7323 (Figs. 3 and 4) shows an enhanced X-ray luminosity ($\approx 10^{36} - 10^{37} \text{ erg s}^{-1}$) at periastron. In a few cases, the source has been detected at high X-ray luminosities (similar to those observed at periastron) across the entire orbit, including orbital phases near to the apastron. Moreover, AX J0049.4–7323

shows a high variability far from periastron, with a maximum variability factor of ~ 270 .

The periodic outbursts at periastron displayed by AX J0049.4–7323 are consistent with the definitions of type I outburst given in Sect. 1. In the framework of the truncation disc model, the system is expected to have a high eccentricity to show regular type I outbursts. On the other hand, the strong X-ray variability and high luminosity states observed out of periastron cannot be reconciled with the typical variability of Be/XRBs, traditionally described in terms of type I and type II outbursts. The same conclusion was reached by Coe & Edge (2004) on the basis of three *ASCA* outbursts ($L_x \approx 10^{35} \text{ erg s}^{-1}$) observed far from periastron. The anomalous X-ray variability of AX J0049.4–7323 noted by Coe & Edge (2004) is confirmed by the results presented in Sect. 3; it is further complicated when the *RXTE* detections reported in Yang et al. (2017) and Klus et al. (2014) are taken into account. Figure 6 shows two interesting *RXTE* detections at $t_a = 55262.10 \text{ MJD}$ and $t_b = 55556.02 \text{ MJD}$ (Yang et al. 2017; Klus et al. 2014). Together with the *Chandra* and *Swift* detections and upper limits reported in Table 3 and shown in Fig. 6, they constitute two peculiar events characterized by high variability and with timescales $t \ll P_{\text{orb}}$, located far from periastron. In particular, from $\sim 55262 \text{ MJD}$ (*RXTE* observation) to $\sim 55300 \text{ MJD}$ (*Chandra* observations), about 90 days before the periastron passage ($\phi_{\text{orb}} \approx 0.8 - 0.9$), the X-ray flux decreased by a factor of ~ 150 in less than about 38 days. *Chandra* observed the source five times in the subsequent 18 days. During this period, AX J0049.4–7323 showed a slow increase in flux, from $\approx 4 \times 10^{-14} \text{ erg cm}^{-2} \text{ s}^{-1}$ to $\approx 10^{-13} \text{ erg cm}^{-2} \text{ s}^{-1}$. After this X-ray dip caught by *Chandra*, AX J0049.4–7323 was observed again by *RXTE*, close to periastron ($\sim 55364 \text{ MJD}$), with a flux of $\approx 4.3 \times 10^{-12} \text{ erg cm}^{-2} \text{ s}^{-1}$. Another jump in luminosity was observed in the subsequent orbital cycle, when AX J0049.4–7323 showed an increase in brightness from $F_x \leq 10^{-13} \text{ erg cm}^{-2} \text{ s}^{-1}$ at $\sim 55542 \text{ MJD}$ (*Swift/XRT*) to $F_x \approx 4 \times 10^{-12} \text{ erg cm}^{-2} \text{ s}^{-1}$ at $\sim 55556 \text{ MJD}$ (*RXTE*, Yang et al. 2017), and then a decrease to $F_x \leq 10^{-13} \text{ erg cm}^{-2} \text{ s}^{-1}$ at $\sim 55607 \text{ MJD}$ (*Swift/XRT*). The peak luminosity was observed close to apastron (at the orbital phase ~ 0.56). The timescale of the variability and the flux levels are similar to those of the previous event. This variability could be ascribed to multiple short-term outbursts peaking randomly in the orbital phase. Hereafter, we consider two possible mechanisms to explain the observed variability.

4.2.1. Gating mechanism

The decrease in luminosity observed during the events reported in Sect. 3 might be caused by the onset of the centrifugal barrier when the mass inflow rate decreases to a certain limiting value. Transitions from direct accretion to centrifugal inhibition of accretion (or propeller, Illarionov & Sunyaev 1975) were proposed by Stella et al. (1986) to explain the high dynamical range, spanning up to six orders of magnitudes, of the X-ray luminosity of some transient Be/XRBs. These transitions depend on the amount of inflowing matter, on the magnetic field strength of the NS and on its spin period. They can be easily understood by introducing the definitions of corotation and magnetospheric radii. The corotation radius (r_c) is the distance from the NS at which there is a balance between the NS angular velocity and the Keplerian angular velocity. For AX J0049.4–7323 we obtain $r_c = (GM_{\text{NS}})^{1/3} (P_s/2\pi)^{2/3} \approx 1.4 \times 10^{10} \text{ cm}$, where we assumed $M_{\text{NS}} = 1.4 M_{\odot}$ and $P_s = 750 \text{ s}$. The magnetospheric radius (r_m) is the distance from the NS where the magnetic field pressure

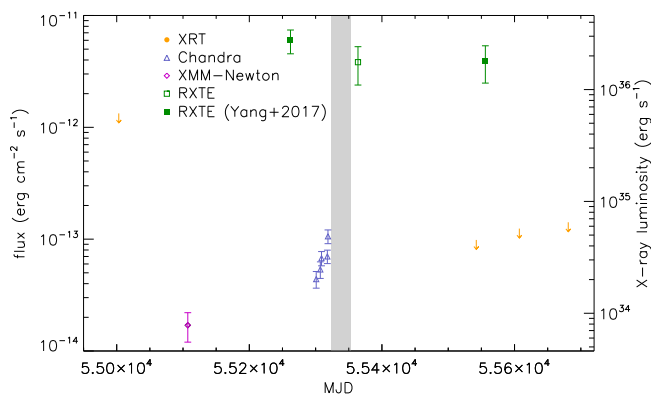


Fig. 6. X-ray light curve of AX J0049.4–7323 around the periastron passage at ≈ 55340 MJD, showing the *RXTE* detections reported in Yang et al. (2017) and Klus et al. (2014) (filled green boxes). The grey vertical stripe shows the time of periastron passage according to the ephemeris calculated by Schmidtke et al. (2013).

equals the ram pressure of the accreted ionized plasma dragged along the field lines. If the magnetospheric radius is pushed inside the corotation radius by a sufficiently high amount of inflowing matter, the matter is expected to be effectively accreted by the NS. If the inflowing matter decreases, for example because of small variations in the wind properties around the NS (density and wind velocity), the magnetospheric radius can expand beyond the corotation radius. In this case, the plasma dragged by the magnetic field lines at the magnetosphere would rotate at a super-Keplerian rate, the magnetosphere would behave as a closed barrier, and direct accretion would be inhibited. According to Stella et al. (1986), the minimum X-ray luminosity caused by direct accretion is obtained assuming $r_m = r_c$, and it is given by

$$L_{\min} = \frac{GM_{\text{NS}}\dot{M}_{\min}}{R} \approx 4 \times 10^{30} R_6^{-1} M_{1.4}^{-2/3} \mu_{30}^2 P_{750}^{-7/3} \text{ erg s}^{-1}, \quad (3)$$

where \dot{M}_{\min} is the minimum mass accretion rate for which the NS accretes directly, $R_6 = 10^6$ cm is the radius of the NS, $M_{1.4} = 1.4 M_{\odot}$ is the mass of the neutron star, $\mu_{30} = 10^{30}$ G cm³ is the NS magnetic moment, and $P_{750} = 750$ s is the spin period of AX J0049.4–7323. In Eq. (3) we assumed a 100 % efficient conversion of the gravitational potential energy of the accreted matter into X-ray radiation. If we assume that the minimum X-ray luminosity caused by direct accretion is the lowest luminosity observed by *XMM-Newton* and *Chandra* when the pulsation was detected (Hong et al. 2017; Haberl et al. 2008), i.e. $L_{\min} \approx 3 \times 10^{35}$ erg s⁻¹, from Eq. (3) we find that the pulsar of AX J0049.4–7323 should have a magnetic field strength of $\approx 2.7 \times 10^{14}$ G. When the centrifugal barrier becomes active ($r_m = r_c$), the maximum allowed luminosity in the propeller regime is given by (see Campana 1997)

$$L_{\max} = \frac{GM_{\text{NS}}\dot{M}_{\min}}{r_c} \approx 2.3 \times 10^{27} \mu_{30}^2 M_{1.4}^{-1} P_{750}^{-3} \text{ erg s}^{-1}, \quad (4)$$

which is of the order of 10^{30} erg s⁻¹ when we assume $B \approx 2.7 \times 10^{14}$ G⁵. The value of L_{\max} found with Eq. 4 is more than three

⁵ The approximated equation 2 for the calculation of the magnetospheric radius in Stella et al. (1986) might lead to overestimating it, as discussed in Bozzo et al. (2009). Therefore, the values given in Eqs. (3) and (4) have to be taken with caution, and could be affected by an uncertainty of a factor of a few.

orders of magnitude lower than the lowest luminosity observed by *XMM-Newton* in October 2009, $L_{\text{lowest}} = 8 \times 10^{33}$ erg s⁻¹. This value of L_{lowest} is about 10–100 times higher than the X-ray luminosity of the brightest known Be stars (Motch et al. 2007), and about 10^3 times higher than the X-ray luminosity of typical Be stars. Therefore, the source of this emission is most likely the NS rather than the Be star. The lack of detection of pulsations in the *Chandra* observations at low luminosity (Sect. 3) might be due to insufficient statistics. To verify this possibility, we performed a timing analysis of the *Chandra* data at the lowest flux ($55300.9 \leq t \leq 55318.6$ MJD) which was not reported in previous works. We used barycentred background subtracted light curves, assuming two different bin sizes: 50 s and 100 s. We searched for periodicities using the Lomb–Scargle periodogram technique as described in Sect. 3.2. We did not detect any significant ($\geq 3\sigma$) pulsating signal in the data. We performed simulations on the two light curves built with different bin sizes (50 s and 100 s) to set a 3σ upper limit on the pulsed fraction of a sinusoidal signal of about 45 %. This upper limit is comparable with the typical pulsed fraction of the source detected at higher luminosities (see e.g. Hong et al. 2017). Therefore, we conclude that the transitions from centrifugal inhibition of accretion to direct accretion is unlikely to be responsible for the observed jumps in X-ray luminosity.

4.2.2. Accretion from a cold disc

Another possibility is given by the scenario proposed by Tsygankov et al. (2017). They showed that, after an outburst, a sufficiently slow pulsar in a Be/XRB could switch to an accretion state in which the pulsar is fed by a cold accretion disc. This accretion state is possible if the mass accretion rate is sufficiently high to open the centrifugal barrier ($r_m < r_c$) and sufficiently low to have an accretion disc colder than ≈ 6500 K. The latter condition is verified if⁶

$$L < L^{\text{cold}} = 9 \times 10^{33} \kappa^{1.5} M_{1.4}^{0.28} R_6^{1.57} B_{12}^{0.86} \text{ erg s}^{-1},$$

where $B_{12} = B/(10^{12}$ G). The magnetic field strength of the pulsar in AX J0049.4–7323 is not known. Assuming four test values, $B_{12} = 10^{12}$, $B_{13} = 10^{13}$, $B_{14} = 10^{14}$ G, and $B_{15} = 10^{15}$ G, we find $L_{12}^{\text{cold}} = 3 \times 10^{33}$ erg s⁻¹, $L_{13}^{\text{cold}} = 2.3 \times 10^{34}$ erg s⁻¹, $L_{14}^{\text{cold}} = 1.7 \times 10^{35}$ erg s⁻¹, and $L_{15}^{\text{cold}} = 1.2 \times 10^{36}$ erg s⁻¹. Tsygankov et al. (2017) also noted that the accretion state (cold disc versus propeller) after an outburst is determined by the spin period and magnetic field strength. Stable accretion from a cold disc, instead of the onset of the propeller regime, is possible if

$$P_{\text{spin}} > P^* = 36.6 \kappa^{6/7} B_{12}^{0.49} M_{1.4}^{-0.17} R_6^{1.22} \text{ s}.$$

Assuming again four possible values for the magnetic field strength of the pulsar, we find $P_{12}^* = 20$ s, $P_{13}^* = 62$ s, $P_{14}^* = 193$ s, and $P_{15}^* = 596$ s. Therefore, the relatively high luminosities of AX J0049.4–7323 observed far from periastron ($L_x \approx 2 \times 10^{35} - 10^{36}$ erg s⁻¹) might be caused by stable accretion from a cold accretion disc only if the magnetic field of the pulsar is high, i.e. $B \gtrsim 10^{14}$ G. Although magnetic fields of this magnitude are possible in accreting NSs in high-mass X-ray binaries,

⁶ Tsygankov et al. (2017) presented accurate conditions to have accretion from a cold disc (see their equations 12 and 13). However, due to the lack of enough information for AX J0049.4–7323, we use here the simplified conditions, based on the assumption that the temperature of the accretion disc reaches its maximum at the inner radius (see equations 6 and 7 in Tsygankov et al. 2017).

they should represent rare cases compared to the typical values measured so far ($B \approx 10^{11-13}$ G, [Revnivtsev & Mereghetti 2015](#)). Therefore, accretion from a cold disc is unlikely to be the reason for the short-term variability at random orbital phases in AX J0049.4–7323.

4.2.3. Perturbed circumstellar disc

If we exclude that the two previous mechanisms are responsible for the high X-ray variability of AX J0049.4–7323, one possibility is that outside the time periods with enhanced X-ray activity ($L_x \geq 10^{35}$ erg s $^{-1}$), AX J0049.4–7323 is a persistent emitter, with luminosity of the order of L_{lowest} . There is a small subclass of Be/XRBs that display persistent X-ray emission at low luminosity levels ($L_x \geq 10^{34} - 10^{35}$ erg s $^{-1}$) and low X-ray variability (compared to Be/XRB transients; see [Reig & Roche 1999](#) and references therein). AX J0049.4–7323 has some properties in common with the class of persistent Be/XRBs, which also contains slowly rotating NSs ($P_{\text{spin}} > 200$ s) in wide orbits ($P_{\text{orb}} > 30$ d; [Reig 2007, 2011](#)). On the other hand, persistent Be/XRBs have low eccentricities ($e < 0.2$), at odds with the high eccentricity inferred for AX J0049.4–7323 to explain the outbursts at periastron (see beginning of this section). Nonetheless, we note that another persistent Be/XRB, RX J0440.9+4431 ($P_{\text{orb}} \approx 150$ d, $P_{\text{spin}} \approx 205$ s), rarely showed flaring activity at periastron (peak luminosity $L_x \approx 7.5 \times 10^{36}$ erg s $^{-1}$, 2–30 keV; [Ferrigno et al. 2013](#)). In this system, the persistent emission ($L_x \approx 5 \times 10^{34}$ erg s $^{-1}$) might be a consequence of the accretion of the rarefied wind produced by the companion star outside the circumstellar disc, while the flares are related to the accretion at periastron of the dense wind of the circumstellar disc ([Ferrigno et al. 2013](#)).

The observed jumps in luminosity might suggest that the material accreted by the NS across the orbit is strongly inhomogeneous, and it is characterized by strong variations in density and stellar wind velocity uncorrelated with the orbital phase. In Sect. 3 we showed that the variability timescales of these jumps is ≤ 37 d. Assuming a circular orbit, an orbital period of 393 d, and masses of the two stars of $M_* = 18 M_{\odot}$ ([Klus et al. 2014](#)) and $M_{\text{NS}} = 1.4 M_{\odot}$, we find that the sizes of the structures responsible for the variability are of the order of 2.5×10^{13} cm. Such large structures encountered by the NS along the orbit might be the result of the tidal interaction of the NS with the circumstellar disc during previous orbital passages. As suggested by [Okazaki & Nequeruella \(2001\)](#), in binary systems with very long orbital periods (≥ 200 d), the Be disc might be able to spread out significantly beyond the truncation radius while the NS is far from periastron. Moreover, three-dimensional hydrodynamic simulations have shown that in a systems with a misaligned orbital plane and a circumstellar disc, a warped and eccentric circumstellar disc can develop ([Martin et al. 2014](#)). We propose that the disc expansion in AX J0049.4–7323 might occur not uniformly on the equatorial plane of the Be star, and when the NS crosses the circumstellar disc again, it might accrete large isolated structures characterized by high density and low wind velocity. It is worth noting that GRO J1008–57, another Be/XRB with a long orbital period (~ 250 d) showed an anomalous variability in 2014/2015, namely three outbursts in a single orbit, with the peak of the third reached at apastron ([Kühnel et al. 2017](#)). [Kühnel et al. \(2017\)](#) discussed the peculiar variability of GRO J1008–57 in the framework of misaligned orbital plane and circumstellar disc, with outbursts occurring at the intersection between these two planes. We point out that variabil-

ity displayed by GRO J1008–57 in 2014/2015, shows some similarities with that observed in AX J0049.4–7323 and presented in this work. Nonetheless, we note that it is difficult to explain the X-ray variability of AX J0049.4–7323 with the scenario proposed for GRO J1008–57. In fact, the high luminosity states of AX J0049.4–7323 observed far from periastron by *ASCA*, *Chandra*, and *RXTE*, always occur at different orbital phases, while the other intersection (at periastron) is constant in phase with time. Such strong variability of the phase at which one of the two intersections occurs would require a warped/tilted or high precessing circumstellar disc.

5. Conclusions and future work

We presented an analysis of archival *Swift*, *Chandra*, *XMM-Newton*, *RXTE*, and *INTEGRAL* data of the Be/XRB AX J0049.4–7323. The spectral analysis shows an anticorrelation between the power law slope describing the X-ray continuum and the X-ray flux. This behaviour has been observed in other accreting pulsars in early-type systems (e.g. [Reig & Nespoli 2013](#); [Romano et al. 2014](#); [Malacaria et al. 2015](#)).

AX J0049.4–7323 shows a secular spin-up of $\dot{P} = (-3.00 \pm 0.12) \times 10^{-3}$ s day $^{-1}$, which suggests that the pulsar has not yet achieved the equilibrium period.

To gain more information about the X-ray properties of AX J0049.4–7323, we studied its long-term X-ray variability, making use of *ASCA*, *Swift*, *Chandra*, *XMM-Newton*, *RXTE*, and *INTEGRAL* data analysed here and in other works. We found that AX J0049.4–7323 shows a high X-ray variability, with high luminosity states ($L_x > 5 \times 10^{35}$ erg s $^{-1}$) caught by *Chandra*, *Swift*, *RXTE*, and *ASCA* far from periastron, which suggests that the NS experienced prolonged periods of relatively high accretion rate in different orbital cycles, likely due to the presence of a stable ($t \geq 1000$ d) extended circumstellar disc. Two *RXTE* detections reported by [Yang et al. \(2017\)](#) and [Klus et al. \(2014\)](#), together with *Chandra* and *Swift* data analysed in this work, would indicate two cases of anomalous fast variability far from periastron. If the *RXTE* detections reported by [Yang et al. \(2017\)](#) and [Klus et al. \(2014\)](#) are not due to spurious effects introduced by statistical fluctuations, we showed that the observed anomalous fast variability discussed in Sect. 3.3 is likely due to complicated tidal interactions of the NS with an extended circumstellar disc. It would be important to observe these flaring events again with future observations. The hypotheses proposed here and in other papers ([Coe & Edge 2004](#)) to explain the long-term variability of AX J0049.4–7323 could be verified through a more continuous X-ray monitoring of the source, coupled with simultaneous spectroscopic observations in optical/UV, especially focused on the study of the long-term variability of emission lines such as H α . This would provide important information about possible changes of the properties of the circumstellar disc, such as its size and orientation.

Acknowledgements. We thank the anonymous referee for the useful comments that improved the manuscript. L.D. thanks Jun Yang for answering some questions about the library of X-ray pulsars in SMC. This paper is based on data from observations with *XMM-Newton*, *Swift*, and *Chandra* X-ray observatory. *XMM-Newton* is an ESA science mission with instruments and contributions directly funded by ESA Member States and NASA. *Chandra* data were obtained from the *Chandra* Data Archive. This paper is based on data from observations with *INTEGRAL*, an ESA project with instruments and science data centre funded by ESA member states (especially the PI countries: Denmark, France, Germany, Italy, Spain, and Switzerland), Czech Republic, and Poland, and with the participation of Russia and the USA. This work is supported by the Bundesministerium für Wirtschaft und Technologie through the Deutsches Zentrum

für Luft und Raumfahrt (grant FKZ 50 OG 1602). P.R. acknowledges contract ASI-INAF I/004/11/0.

References

- Arnaud, K. A. 1996, in *Astronomical Society of the Pacific Conference Series*, Vol. 101, *Astronomical Data Analysis Software and Systems V*, ed. G. H. Jacoby & J. Barnes, 17
- Baykal, A., Stark, M. J., & Swank, J. H. 2002, *ApJ*, 569, 903
- Bozzo, E., Stella, L., Vietri, M., & Ghosh, P. 2009, *A&A*, 493, 809
- Burrows, D. N., Hill, J. E., Nousek, J. A., et al. 2005, *Space Sci. Rev.*, 120, 165
- Camero, A., Zurita, C., Gutiérrez-Soto, J., et al. 2014, *A&A*, 568, A115
- Campana, S. 1997, *A&A*, 320, 840
- Cash, W. 1979, *ApJ*, 228, 939
- Coe, M. J., Bird, A. J., Buckley, D. A. H., et al. 2010, *MNRAS*, 406, 2533
- Coe, M. J. & Edge, W. R. T. 2004, *MNRAS*, 350, 756
- Cowley, A. P. & Schmidtke, P. C. 2003, *AJ*, 126, 2949
- Dickey, J. M. & Lockman, F. J. 1990, *ARA&A*, 28, 215
- Edge, W. R. T. & Coe, M. J. 2003, *MNRAS*, 338, 428
- Ferrigno, C., Farinelli, R., Bozzo, E., et al. 2013, *A&A*, 553, A103
- Galache, J. L., Corbet, R. H. D., Coe, M. J., et al. 2008, *ApJS*, 177, 189
- Gehrels, N., Chincarini, G., Giommi, P., et al. 2004, *ApJ*, 611, 1005
- Glotfelty, K. 2014, in *15 Years of Science with Chandra, Posters from the Chandra Science Symposium held 18-21 November, 2014 in Boston, MA.*, id.P21, P21
- Haberl, F., Eger, P., & Pietsch, W. 2008, *A&A*, 489, 327
- Haberl, F. & Pietsch, W. 2004, *A&A*, 414, 667
- Hong, J., Antoniou, V., Zezas, A., et al. 2017, *ApJ*, 847, 26
- Horne, J. H. & Baliunas, S. L. 1986, *ApJ*, 302, 757
- Ikhsanov, N. R. 2007, *MNRAS*, 375, 698
- Ikhsanov, N. R., Jordan, S., & Beskrovnaya, N. G. 2002, *A&A*, 385, 152
- Illarionov, A. F. & Sunyaev, R. A. 1975, *A&A*, 39, 185
- Jahoda, K., Swank, J. H., Giles, A. B., et al. 1996, in *Proc. SPIE, Vol. 2808, EUV, X-Ray, and Gamma-Ray Instrumentation for Astronomy VII*, ed. O. H. Siegmund & M. A. Gummin, 59–70
- Kalberla, P. M. W., Burton, W. B., Hartmann, D., et al. 2005, *A&A*, 440, 775
- Kennea, J. A., Evans, P. A., & Coe, M. J. 2016, *The Astronomer’s Telegram*, 9299
- Klus, H., Ho, W. C. G., Coe, M. J., Corbet, R. H. D., & Townsend, L. J. 2014, *MNRAS*, 437, 3863
- Kraft, R. P., Burrows, D. N., & Nousek, J. A. 1991, *ApJ*, 374, 344
- Kühnel, M., Fürst, F., Pottschmidt, K., et al. 2017, *A&A*, 607, A88
- Laycock, S., Corbet, R. H. D., Coe, M. J., et al. 2005, *ApJS*, 161, 96
- Lebrun, F., Leray, J. P., Lavocat, P., et al. 2003, *A&A*, 411, L141
- Malacaria, C., Klochkov, D., Santangelo, A., & Staubert, R. 2015, *A&A*, 581, A121
- Martin, R. G., Nixon, C., Armitage, P. J., Lubow, S. H., & Price, D. J. 2014, *ApJ*, 790, L34
- McBride, V. A., Coe, M. J., Negueruela, I., Schurch, M. P. E., & McGowan, K. E. 2008, *MNRAS*, 388, 1198
- Motch, C., Lopes de Oliveira, R., Negueruela, I., Haberl, F., & Janot-Pacheco, E. 2007, in *Astronomical Society of the Pacific Conference Series, Vol. 361, Active OB-Stars: Laboratories for Stellar and Circumstellar Physics*, ed. A. T. Okazaki, S. P. Owocki, & S. Stefl, 117
- Negueruela, I. & Okazaki, A. T. 2001, *A&A*, 369, 108
- Okazaki, A. T. & Negueruela, I. 2001, *A&A*, 377, 161
- Press, W. H. & Rybicki, G. B. 1989, *ApJ*, 338, 277
- Reig, P. 2007, *MNRAS*, 377, 867
- Reig, P. 2011, *Ap&SS*, 332, 1
- Reig, P. & Nespoli, E. 2013, *A&A*, 551, A1
- Reig, P. & Roche, P. 1999, *MNRAS*, 306, 100
- Revnitsev, M. & Mereghetti, S. 2015, *Space Sci. Rev.*, 191, 293
- Romano, P., Ducci, L., Mangano, V., et al. 2014, *A&A*, 568, A55
- Roming, P. W. A., Kennedy, T. E., Mason, K. O., et al. 2005, *Space Sci. Rev.*, 120, 95
- Schmidtke, P. C., Cowley, A. P., & Udalski, A. 2013, *MNRAS*, 431, 252
- Stella, L., White, N. E., & Rosner, R. 1986, *ApJ*, 308, 669
- Tsygankov, S. S., Mushtukov, A. A., Suleimanov, V. F., et al. 2017, *A&A*, 608, A17
- Ubertini, P., Lebrun, F., Di Cocco, G., et al. 2003, *A&A*, 411, L131
- Ueno, M., Yokogawa, J., Imanishi, K., & Koyama, K. 2000, *IAU Circ.*, 7442
- Yang, J., Laycock, S. G. T., Christodoulou, D. M., et al. 2017, *ApJ*, 839, 119
- Yokogawa, J., Imanishi, K., Ueno, M., & Koyama, K. 2000, *PASJ*, 52, L73